



This is a repository copy of *Surface topographic impact of subglacial water beneath the south polar ice cap of Mars*.

White Rose Research Online URL for this paper:

<https://eprints.whiterose.ac.uk/191667/>

Version: Accepted Version

Article:

Arnold, N.S., Butcher, F.E.G. orcid.org/0000-0002-5392-7286, Conway, S.J. et al. (2 more authors) (2022) Surface topographic impact of subglacial water beneath the south polar ice cap of Mars. *Nature Astronomy*, 6 (11). pp. 1256-1262. ISSN 2397-3366

<https://doi.org/10.1038/s41550-022-01782-0>

This is a post-peer-review, pre-copyedit version of an article published in *Nature Astronomy*. The final authenticated version is available online at:
<http://dx.doi.org/10.1038/s41550-022-01782-0>.

Reuse

Items deposited in White Rose Research Online are protected by copyright, with all rights reserved unless indicated otherwise. They may be downloaded and/or printed for private study, or other acts as permitted by national copyright laws. The publisher or other rights holders may allow further reproduction and re-use of the full text version. This is indicated by the licence information on the White Rose Research Online record for the item.

Takedown

If you consider content in White Rose Research Online to be in breach of UK law, please notify us by emailing eprints@whiterose.ac.uk including the URL of the record and the reason for the withdrawal request.



eprints@whiterose.ac.uk
<https://eprints.whiterose.ac.uk/>

1 Surface topographic impact of subglacial water beneath Mars'
2 south polar ice cap

3 N.S. Arnold^{1*}, F.E.G. Butcher^{2*}, S.J. Conway³, C. Gallagher⁴ and M.R.
4 Balme⁵

5 1. Scott Polar Research Institute, University of Cambridge, Lensfield
6 Road, Cambridge, CB2 1ER, UK.

7 2. Department of Geography, The University of Sheffield, Winter Street,
8 Sheffield, S10 2TN, UK

9 3. CNRS, UMR 6112 Laboratoire de Planétologie et Géodynamique,
10 Université de Nantes, France

11 4. UCD School of Geography, Newman Building, University College Dublin,
12 Belfield, Dublin 4, Ireland, and UCD Earth Institute, University College
13 Dublin, Belfield, Dublin 4, D04 V1W8, Ireland.

14 5. School of Physical Sciences, The Open University, Walton Hall, Milton
15 Keynes MK7 6AA, UK

16 *. Corresponding Authors: NA: nsa12@cam.ac.uk. FEGB:
17 f.butcher@sheffield.ac.uk

18 **Bright radar reflections observed at the Ultimi Scopuli region of**
19 **Mars' south polar layered deposits (SPLD) ^{1,2,3} by the Mars**
20 **Advanced Radar for Subsurface and Ionosphere Sounding**
21 **(MARSIS) instrument have been interpreted as the signature of**
22 **areas of subglacial water beneath it. However, other studies put**
23 **forward alternative explanations that do not imply the presence of**
24 **liquid water^{4,5,6}. Here we shed light on the issue by looking at the**
25 **surface topography of the region. On Earth, reduced or absent**
26 **basal friction, and consequent ice velocity changes, cause a**
27 **distinct topographic signature over subglacial lakes⁷. Using Mars**
28 **Orbiter Laser Altimeter (MOLA) data, ⁸ we identify and**
29 **characterise an anomaly in the surface topography of the SPLD**
30 **overlying the area of the putative lakes, similar to those found**
31 **above terrestrial subglacial lakes of similar size. Ice flow model**
32 **results suggest comparable topographic anomalies form within**
33 **0.5 – 1.5 Myr with locally elevated geothermal heating⁹ or 2 – 5**
34 **Myr without elevated geothermal heating². These findings offer**
35 **independent support for the presence of basal water beneath**

Ultimi Scopuli and suggest surface topography could supplement radar returns to help identify other potential subglacial water bodies.

Main

Ice deposits on planetary surfaces raise the temperature at the ice/bedrock interface, as geothermal heat must be conducted through the ice rather than being lost directly at the bedrock surface. Frictional heat produced by flowing ice is concentrated at the base of the ice mass¹⁰, further warming the ice/bedrock interface. On Earth, many glacier beds reach the pressure melting point, and subglacial lakes are widespread; hundreds have been identified beneath the Antarctic Ice Sheet¹¹, and over 50 beneath the Greenland ice sheet¹¹. Whilst there is evidence for past subglacial water beneath an ancient south polar ice sheet on Mars^{12,13}, and more recent water (100s Myr ago) beneath some existing mid-latitude ice deposits^{14,10,15,23}, it is widely assumed that Mars' present-day ice deposits are frozen throughout under cold, dry contemporary climate conditions.

This assumption has been questioned by the areas of bright basal radar reflections in MARSIS data from Ultimi Scopuli, centred around 81°S, 193°E (Fig. 1a), which have been taken to be indicative of one¹, or multiple² subglacial water bodies (likely in the form of saturated perchlorate brines^{1,2,9,16}). Additional areas of high basal reflected radar power across the SPLD³ also potentially indicate more widespread basal water. The liquid water explanation for the bright radar reflections is contested, however. Local changes in the electrical conductivity of the substrate could be a cause⁴, potentially due to liquid brines, metal-bearing minerals, saline ice, or cold, hydrated smectite clays⁵. Such deposits occur in the highlands surrounding the SPLD, and are argued to be likely to occur, and be detectable, beneath the SPLD^{4,5,6}. However, analyses of the MARSIS data alone have not confirmed either a liquid or solid interpretation for the bright basal radar reflections.

Subglacial lakes are commonly identified on Earth using ice penetrating radar. However, a small number have been identified by their influence on the surface topography^{7,17,18}. Reduced basal friction and consequent ice velocity changes over basal water (particularly lakes) lead to the development of flat areas on ice surfaces over large lakes (e.g. Lake Vostok), with extensional flow at the upstream margin causing surface lowering, and compressional flow at the downstream margin causing a

surface rise⁷. Smaller lakes (~10 – 20 km in size) seem not to develop the large flat area, but still show a distinctive undulation along the ice flowline over the lake⁷.

Here, we have identified a local anomaly in the Mars Orbiter Laser Altimeter (MOLA) SPLD surface topography⁸ over the area of inferred subglacial water in Ultima Scopuli¹. The regional MOLA topography (Fig. 1b) is generally planar away from a surface depression ~60 km to the south of the inferred water, and the large asymmetric polar scarps (LAPS¹⁹) ~30 km to the north-west. The general topographic trend is a gentle slope (~0.15°) towards the ice edge to the north-east (average azimuth ~66° clockwise from N). However, topographic analysis techniques sensitive to subtle, local variations (Methods) show a clear anomaly proximal to the inferred water bodies. Slope-shading²⁰ reveals a distinct feature (white arrows in Fig. 1c) trending through the centre of the region towards the LAPS to the north-west. Linear trend surface analysis over the central 30 km radius area shows a strong fit ($R^2 = 0.994$, $P < 10^{-6}$), but with significant spatial autocorrelation (Moran's $I = 0.972$, $P < 0.001$) in the residuals (Fig. 1d). There is a raised WNW-ESE-oriented 'bench' (a, Fig. 1d) up to 7 m above the trend surface, located just off-centre to the ESE of the area of inferred water¹, with an associated topographic depression up to 4 m below the trend surface (b, Fig. 1d) ~10 – 15 km up-slope of the bench. There are also two local lows near the E and SW edges of the region (c and d, Fig. 1d); the residuals near the NW edge of the area are affected by the nearby LAPS (yellow arc, Fig 1d). Contributing area algorithm²¹ results (Fig. 1e) show a clear diversion in the steepest downhill slope direction near the centre of the region due to the presence of the bench and depression.

The height differences from the regional trend over the bench and depression, along the ice flow direction, are very similar to those observed (~ +/- 5 – 10 m) over small (10 – 20 km diameter) Antarctic lakes⁷. They are small compared with the overall elevation range of ~200 m across the 30 km radius area, but given the vertical precision of the MOLA instrument (<1 m)⁸ and low overall slopes in the area, our analysis shows that they alter the local surface elevation, slope and aspect sufficiently to appear both as coherent areas of similar trend surface residuals and to cause the clear deviation in the direction of steepest slope seen in the contributing area results. By contrast, the depressions visible in the residuals at the edge of the area (Fig. 1d c and d) do not affect contributing area results.

Given the cold temperature of the SPLD and lower Martian gravity, the question remains as to whether absent basal friction over water bodies could lead to a surface topographic effect, or if flow is too slow, or the ice too thick, for a detectable effect. To assess the possibility that the anomalies reported here could result from subglacial water, we conducted a series of experiments using a high-order numerical ice flow model, the Ice Sheet and Sea Level System Model (ISSM²², Methods) allowing basal sliding over the inferred water bodies^{1,2}. Given the likely influence of MARSIS radar track orientation and spacing on inferred shape and extent of the inferred water areas, we also conduct experiments with two synthetic shapes: a circular water body 10 km in radius (similar in size to the first-identified water body¹), and a lozenge-shaped water body located just up-ice of the topographic bench, and of comparable shape and area (Methods). The generation of subglacial water within the region probably required locally elevated geothermal flux (GHF)^{9,23}, which affects ice viscosity and thus ice flow. We explored the effect of GHF varied between a nominal background value (30 mWm⁻²) and a maximum of 90 mWm⁻², over a variable radius (20 – 40 km) area surrounding the inferred water body(-ies). This encompasses the range of GHF anomalies investigated by Sori and Bramson⁹, exceeding the 72 mWm⁻² they find necessary to raise the basal ice to ~200K, just above the lowest melting point among the saturated perchlorate brine species (Ca) they investigate. Details of all model runs are given in Supplementary Table 1.

Model results (Fig. 2) show that altered basal friction and/or elevated GHF can produce changes in surface topography, comparable to those observed, within 500 kyr – 1.5 Myr. This is similar to the modelled duration of local GHF elevation due to magma chamber emplacement⁹. We find a GHF of 60 mWm⁻² is the minimum needed to raise the modelled basal temperature to ~200K, lower than the 72 mWm⁻² reported by Sori and Bramson⁹, due to the additional effect of strain-induced heating under enhanced flow¹⁰. We therefore focus mainly on model runs using 60 mWm⁻² GHF as this requires the smallest heat anomaly.

Elevation changes of ~ +/- 5 m occur in 500 kyr in the largest central area of inferred water² with the highest GHF, 90 mWm⁻², applied over a 40 km radius (Fig. 2a; Run M1, Supplementary Table 1). Elevation changes of ~ +/- 3 m are produced in 1.5 Myr when sliding is allowed over the single water body¹, with 60 mWm⁻² GHF over a 20 km radius (Fig. 2b, Run S9). The synthesised 10 km radius circular water area gives elevation changes of ~ +/- 5 m in 1 Myr with 60 mWm⁻² GHF over a 30 km radius (Fig 2c, Run C3). With 60 mWm⁻² GHF over an expanded

lozenge-shaped area equivalent in area to a 30km radius circle (Methods), the synthesised lozenge-shaped water area produces $\sim \pm 4$ m elevation changes in 1 Myr (Fig. 2d, Run LL6). Without additional GHF, allowing basal sliding over the inferred water is sufficient for surface elevation changes of comparable magnitude to those observed to occur within 2 – 5 Myr. The shape of the modelled water (zero friction) area strongly influences the shape of the area in which elevation changes occur; the amount of surface elevation change scales with the area of altered friction, and with the magnitude and spatial extent of additional GHF (Supplementary Information).

Figure 3 shows scatter diagrams of the trend surface residuals (Fig. 1d) versus modelled elevation changes for the runs in Figure 2 for the 824 model grid points within a 20 km radius of the centre of the inferred wet area(s). All models produce significant relationships; R^2 values vary between 0.05 (Run M1) and 0.49 (Run LL6). The R^2 values are affected by areas away from the inferred water areas which exhibit very low modelled elevation change, but have non-zero residuals, visible as horizontal clusters of points in Figure 3. The correspondence between the edges of the high radar reflectance areas and the orientation and spacing of the MARSIS satellite tracks in the region also suggest that the edges of the inferred water bodies are uncertain, affecting the spatial correspondence between model results and the surface topographic anomaly.

The higher predictive power of models with a single area of inferred water, compared to the model with multiple inferred water bodies, suggests that a single area of water best matches the topographic anomaly. Other than for model run M1, the smaller modelled elevation changes in Fig. 2 compared with the topographic anomaly, and shallower than 1:1 relationships in Fig. 3, suggest either $\text{GHF} > 60 \text{ mWm}^{-2}$ may be needed, or that GHF may need to remain elevated for > 1 Myr.

Given the excellent regional MOLA point coverage (Methods), the fact that the anomaly is unique in spatial coherence and extent in the area investigated suggests it is not a data artifact, but a real feature. The anomaly is located very close to the largest² and first identified¹ inferred water body, which shows the brightest radar reflections, highest acuity, and dielectric permittivity, making its interpretation as liquid the most secure. The elongate shape of the anomaly, and best statistical match for model run LL6, may suggest the geothermal heat source could have a more linear shape, as would be associated with an igneous dyke. A

192 difference in water-body shape from that suggested by the radar returns
193 is likely due to uncertainties in the true edge position of the high radar
194 reflectance areas due to MARSIS track orientation and spacing.

195 The rates of elevation change we find are low (peak values of < 0.02
196 mmyr^{-1}), but given the large uncertainties in SPLD surface age estimates
197 ($\sim 10\text{s Myr} - \sim 100\text{s Myr}^{24,25}$), they could sufficiently influence the
198 topography over the time period suggested for elevated geothermal
199 heating due to magma emplacement⁹.

200 Our results suggest that analysis of Mars' SPLD surface topography could
201 assist in identifying which areas of bright radar reflections³ in MARSIS
202 data could be explained by subglacial water bodies, and which may be
203 due to solid materials. If other areas of bright radar reflections show no
204 topographic anomaly, this could make a general explanation for high
205 reflected radar power based on different solid materials more likely. This
206 would make Ultimi Scopuli unique in containing both bright basal radar
207 reflections^{1,2} and a surface topographic signature indicative of an area of
208 zero basal friction. If other areas of bright radar reflections also show
209 surface topographic changes, it may be that basal water occurs more
210 commonly beneath the SPLD, making the long-term presence of brines at
211 sub-eutectic temperatures a possible explanation².

212 Our analysis of the surface topography over an area of subglacial water
213 inferred from MARSIS data shows the first evidence for subglacial water
214 beneath Mars' SPLD that is independent of MARSIS data. Through the
215 combination of the topographic anomaly we identify, numerical model
216 experiments showing the impact of subglacial water on surface
217 topography, and the MARSIS data itself, our results suggest subglacial
218 liquid water generated by local geothermal heating is the most likely
219 explanation for the bright basal radar returns in the Ultima Scopuli area of
220 Mars' SPLD.

221 Methods

222 *Topographic analysis*

223 For all topographic analyses, we use the Mars Orbiter Laser Altimeter
224 (MOLA) surface topography for the south polar region at a resolution of
225 256 pixels per degree (~230m ground resolution)⁸. We checked the MOLA
226 point distribution in the study area; the tracks ran both normal and
227 parallel to the anomaly, and the largest point-to-point spacing is very
228 similar to the DEM grid size. Thus, we expect the DEM to be free of
229 interpolation errors in the study area.

230 *Slope shading*

231 Slope-shading, in which subtle shading depending on local slope and
232 aspect is added to contour maps, is commonly used to emphasise relief to
233 aid visual interpretation of elevation data. We calculate a shading value
234 (ζ) from the local surface slope (S) and aspect (A), and the inclination (I)
235 and declination (D) of the assumed illumination vector following
236 Kennelly²⁰.

$$237 \quad \zeta = \cos(I) \sin(S) \cos(A-D) + \sin(I) \cos(S) \quad (1)$$

238 We illuminate the image from the left of the DEM as shown in the figures,
239 at an angle of 30° above horizontal, and apply a 2.5 x vertical
240 exaggeration.

241 *Trend Surface Analysis*

242 To quantify local elevation deviations from an assumed regional surface,
243 we fit a linear trend surface for MOLA elevation, using polar stereographic
244 grid coordinates, over the area within a 30 km radius of the centre of the
245 inferred water body¹ in order to minimise the influence of the LAPS on the
246 trend surface, and focus on the area containing the inferred water bodies.
247 Residual values show deviations from the trend surface, with negative
248 values showing local lowering. To show spatial autocorrelation in the
249 residuals we calculate Moran's I , using a simple 8-neighbour adjacency
250 matrix with horizontal and vertical weights set to 1, and corner weights
251 set to $1/\sqrt{2}$.

252 *Contributing Area*

253 We use a contributing area algorithm to demonstrate deviations in surface
254 topography; such algorithms are commonly used in hydrological analysis
255 of topography. Each cell in the surface DEM is assigned a value based on
256 its own area, plus the total area of all cells upslope of the original cell for
257 which the lines of steepest descent pass through the cell. The algorithm

we use²¹ passes its calculated area to the single steepest downhill cell (known as a D8 algorithm) and preserves connectivity through closed depressions in the DEM by identifying the lowest cell in the ridge surrounding any closed depressions within the DEM, and routing the area feeding such depressions over this spill-point into the next cell downslope. Contributing area algorithms clearly identify the main potential drainage axes within the topography, as contributing area values at the bottom of valleys (where river channels would be expected to be located on Earth) are much larger than the surrounding cells on valley sides or ridges. The route of such drainage axes is very sensitive to changes in the local slope and aspect.

Ice Flow Modelling

We use the Ice Sheet and Sea Level System Model (ISSM²²) to model ice flow. This is a fully-thermomechanically coupled, finite-element, higher order ice flow model which can be used in a variety of modes of increasing complexity. For our experiments, we use the implementation of the Blatter-Pattyn simplifications of the Stokes Equations within ISSM²². Initial experiments showed no discernible difference between this simplification and a full solution to the Stokes equations, but made a considerable saving in computing time, enabling a larger suite of runs to be performed. We use the MOLA topography (as above) for the ice sheet surface, and the Mars Advanced Radar from Subsurface and Ionosphere Sounding (MARSIS) basal topography²⁶, supplemented in the region of the water bodies by the 'mean perturbed' topography from Arnold et al.²³

We define the model domain by identifying the ice divide surrounding the area containing the water bodies using the contributing area algorithm. We identify all cells within the area covered by the late Amazonian polar cap (IApc) unit²⁷ for which the line of steepest descent passes through the area containing the water bodies, and the cells downstream, in a similar way to a modelling study of ice flow over Lake Vostok, Antarctica²⁸. Mesh resolution is set to 1 km within 30 km of the location of the water bodies, and 10 km elsewhere. Model parameters are given in Supplementary Table 2.

To initialise the model, we first perform a steady-state calculation of the stress balance and resulting ice velocity within the model domain assuming the ice is at the surface temperature throughout, with zero basal sliding allowed. The calculated isothermal velocity is then used as an input into a steady-state, thermally coupled run which is used to calculate the steady-state temperature within the domain. This calculates

the basal temperature, and allows for the softening effect of geothermal heat and internal strain heating on the ice. Given the uncertainty in the SPLD surface mass balance, these runs assume zero surface mass balance. We then use the temperature and ice velocity results of the steady-state, thermally coupled run as additional input values in a transient (time-dependent) run for 1000 model years, again with zero surface mass balance. We use the negative of modelled surface height change over this period as the assumed surface mass balance (so a surface lowering becomes a positive mass balance and vice versa) in the subsequent main model experiments to eliminate as far as possible any background flow-induced effect on the long-term evolution of the surface topography. Modelled changes in surface topography in the main experiments are therefore due to changes in ice flow induced by the assumed basal friction and/or geothermal heat flux changes. Model basal topography and ice thickness data, and the calculated steady-state basal temperature, ice velocity and implied surface mass balance used to initialise the dynamic runs, are shown in Supplementary Figure 1.

For the main model experiments, we allow basal sliding (using the standard basal friction parameterization in ISSM, setting the friction coefficient to zero, implicitly assuming the water body is deep enough to completely detach the basal ice from the bed) over the inferred area of basal water for each model run. We perform four main sets of experiments. 'M' runs allow sliding over the areas with dielectric permittivity > 15 digitised from Figure 5 in Lauro et al.²; 'S' runs allow sliding over the area digitised from the area of positive normalised basal echo power identified by Orosei et al.¹, Figure 3B. The MARSIS radar track spacing and orientation likely influence the spatial interpolation of the inferred areas of liquid (shown by the correspondence between the edges of the high radar reflectance areas identified and the orientation of the satellite tracks in the region), potentially affecting their inferred shape. Therefore, we also perform a set of runs with a synthetic circular area (radius 10 km) of zero friction ('C runs'), centred over the similarly-sized high radar reflectance area identified by Orosei et al.¹, and with a lozenge-shaped area of zero friction ('L runs') based on the shape and area of the topographic bench we identify (Fig. 1c), offset by 5 km up-ice. Outlines of the inferred zero-friction areas can be seen in Figure 2. We also apply a local elevated geothermal heat flux in a variable radius (20 km to 40 km) area centred on the inferred water bodies, up to a maximum value of 90 mWm^{-2} , covering the range of heat fluxes required to achieve basal melt, as modelled by Sori and Bramson⁹. For run LL6 we use an enlarged lozenge shaped area of elevated geothermal heating with

equivalent area to a 30km radius circular area (Fig. 2d). Additional model outputs for Runs M1 and S9 (Figs. 2a-b and 3a-b) are shown in Supplementary Figure 2.

Model duration is initially set to 1 Myr, but for runs with spatially-limited basal sliding and/or lower geothermal heat we extend this to 10 Myr. We undertook some additional 'C' runs to investigate the assumed ice density and thermal conductivity (reflecting the uncertainty in these values, and the range used in other modelling studies of Martian ice masses). We also performed two runs with no sliding, with and without additional geothermal heating; the latter run allowing us to check any possible influence of ice flow alone on topography. Full details of the model runs are given in Supplementary Table 1, and additional details of model inputs and results are given in the Supplementary Information and Supplementary Figures 1 - 2.

352 Data Availability

353 MOLA and MARSIS data are available from the PDS Geosciences node
354 at <http://pds-geosciences.wustl.edu/missions/mgs/megdr.html> and at
355 https://pds-geosciences.wustl.edu/missions/mars_express/marsis.htm
356 respectively; MARSIS data are also available at the ESA Planetary Science
357 Archive ([https://archives.esac.esa.int/psa/#!Ta-](https://archives.esac.esa.int/psa/#!Ta-ble%20View/MARSIS=instrument)
358 [ble%20View/MARSIS=instrument](https://archives.esac.esa.int/psa/#!Ta-ble%20View/MARSIS=instrument)). The 'mean perturbed' bed
359 topography²³ data used in the area containing the inferred water bodies is
360 available via the University of Cambridge Apollo repository at
361 <https://doi.org/10.17863/CAM.41622>.

362 Code Availability

363 ISSM is available from NASA/JPL at <https://issm.jpl.nasa.gov>. Code used
364 to calculate slope shading and contributing area are available by
365 reasonable request to the corresponding author.

366 Acknowledgements

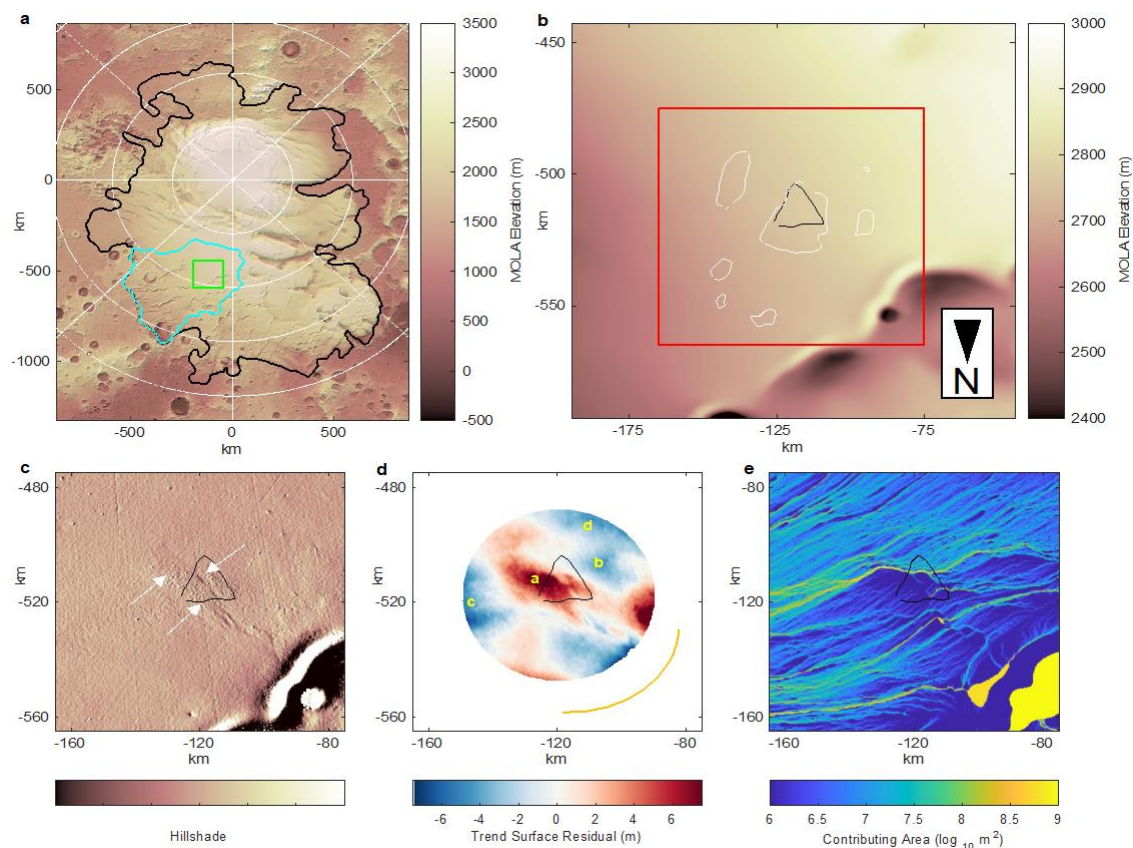
367 The MARSIS instrument and experiment were funded by the Italian Space
368 Agency and NASA. It was developed by the University of Rome, Italy, in
369 partnership with NASA's Jet Propulsion Laboratory [JPL], Pasadena, CA.
370 The Mars Express and Mars Global Surveyor missions are operated by the
371 space agencies of Europe (European Space Agency), Italy (Agenzia
372 Spaziale Italiana) and the United States (NASA). FB is part of the
373 PALGLAC team of researchers and received funding from the European
374 Research Council (ERC) under the European Union's Horizon 2020
375 research and innovation programme (Grant agreement No. 787263). We
376 thank Mathieu Morlighem for help and discussions with ISSM installation
377 and setup.

378 Author Contribution

379 Topographic analysis and modelling was undertaken by NA. FB and SC
380 assisted with MOLA and MARSIS data download and processing, and with
381 initial discussions on the possibility of detecting surface anomalies on the
382 SPLD. CG and MB extracted and processed the original MOLA point data
383 from the repository and checked coverage in the study area. The initial
384 draft of the MS was written by NA; all authors contributed to the
385 submitted version, revisions, and to discussions on the aims and
386 arguments within the paper.

387 Competing Interests

388 The authors declare no competing interests.



390

391 **Figure 1. Surface topography of Mars' South Polar Layered**
392 **Deposit, and topographic analysis results. a.** Regional SPLD MOLA
393 Topography⁸. Black outline shows the outline of the late Amazonian polar
394 cap (IAPC) unit²⁷. Cyan outline shows model domain (Methods); green
395 outline shows the region containing the inferred subglacial water bodies
396 shown in b. **b.** MOLA topography of the area shown by the green box in a.
397 Black outline shows the single inferred subglacial water body¹ and the
398 white outlines show the inferred multiple water bodies². Red square
399 denotes the area shown in c and d. **c.** Hill-shade (Methods) of the area
400 shown by the red square in b. White arrows show the topographic
401 anomaly. **d.** Residuals from linear trend surface analysis over the 30 km
402 radius region centred on the inferred water area. Letters a to d show
403 areas of spatially autocorrelated residuals discussed in the text. Yellow arc
404 shows the location of the nearby LAPS. Black outline as b. **e.** Contributing
405 area map (see Methods) showing the surface area upstream of any given
406 point. Black outline as b. The main axes of high contributing area (yellow)
407 deviate from the general regional north-easterly direction by kinking
408 around the area of positive residuals (a in panel c) before reverting to the
409 regional trend down-slope. Yellow areas in the NW are due to topographic

410 lows associated with the LAPS. Maps use MOLA polar stereographic
411 projection data at 256 pixels per degree (~ 230 m per pixel); X and Y axis
412 labels are coordinates in km. Note that for b – e, north is towards the
413 bottom edge, comparable with figures in Orosei et al.¹ and Lauro et al.²

414

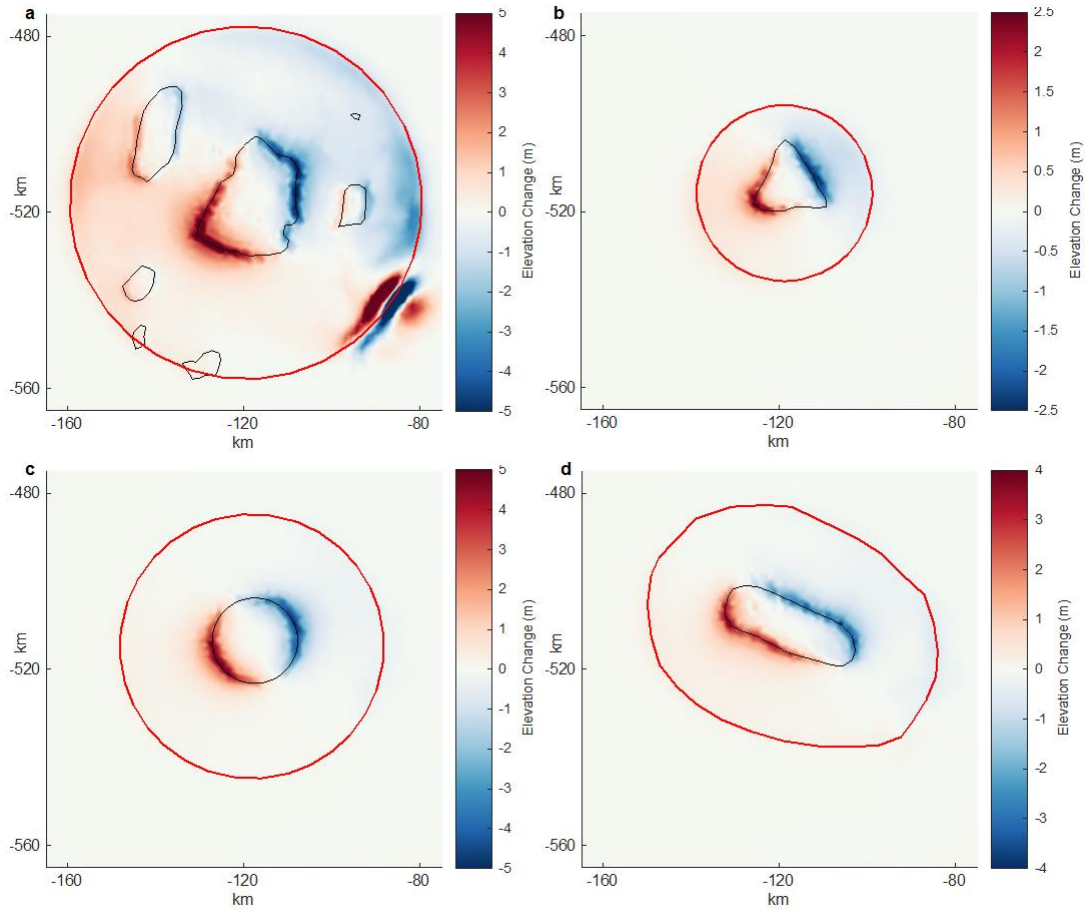


Figure 2. Model results for the centre of the region containing the inferred water (red box in Fig. 1b). **a.** Results from run M1 (Methods) allowing basal sliding over multiple water bodies² (black outlines), with 90 mWm⁻² GHF over a 40km radius (red outline), after 500,000 model years. Maximum rate of change in elevation of $+1.7 \times 10^{-5} \text{ myr}^{-1}$ / $-1.7 \times 10^{-5} \text{ myr}^{-1}$ is reached $\sim 150 \text{ kyr}$ after the onset of heating. The effect of temperature-induced softening of the ice due to high GHF can be seen around the edge of the heated area, with surface lowering up-slope and surface raising down-slope. The large height changes in the NW corner are due to the increase in ice velocity caused by softening over the steep slopes of the LAPS. **b.** Results from run S9 allowing sliding over the single central water body¹ (black outline), with 60 mWm⁻² GHF over a 20 km radius (red outline) after 1 Myr. Maximum rate of elevation change of $+1.7 \times 10^{-6} \text{ myr}^{-1}$ / $-1.7 \times 10^{-6} \text{ myr}^{-1}$ occurs $\sim 200 \text{ kyr}$ after the onset of heating. **c.** Results from run C6 allowing sliding over a 10km radius circular region (black outline), with 60 mWm⁻² GHF over a 30 km radius area (red line) after 1 Myr. Maximum rate of elevation change of $+4.8 \times 10^{-6} \text{ myr}^{-1}$ / $-4.6 \times 10^{-6} \text{ myr}^{-1}$ occurs $\sim 200 \text{ kyr}$ after the onset of heating. **d.** Results from run LL6 allowing sliding over a lozenge-shaped water body (black outline), with 60 mWm⁻² GHF applied within red outline

436 (Methods). Maximum rate of elevation change of $+ 3.3 \times 10^{-6} \text{ myr}^{-1}$ / -
437 $3.6 \times 10^{-6} \text{ myr}^{-1}$ occurs $\sim 200 \text{ kyr}$ after the onset of heating. X and Y axes,
438 and figure orientation as Fig. 1.

439

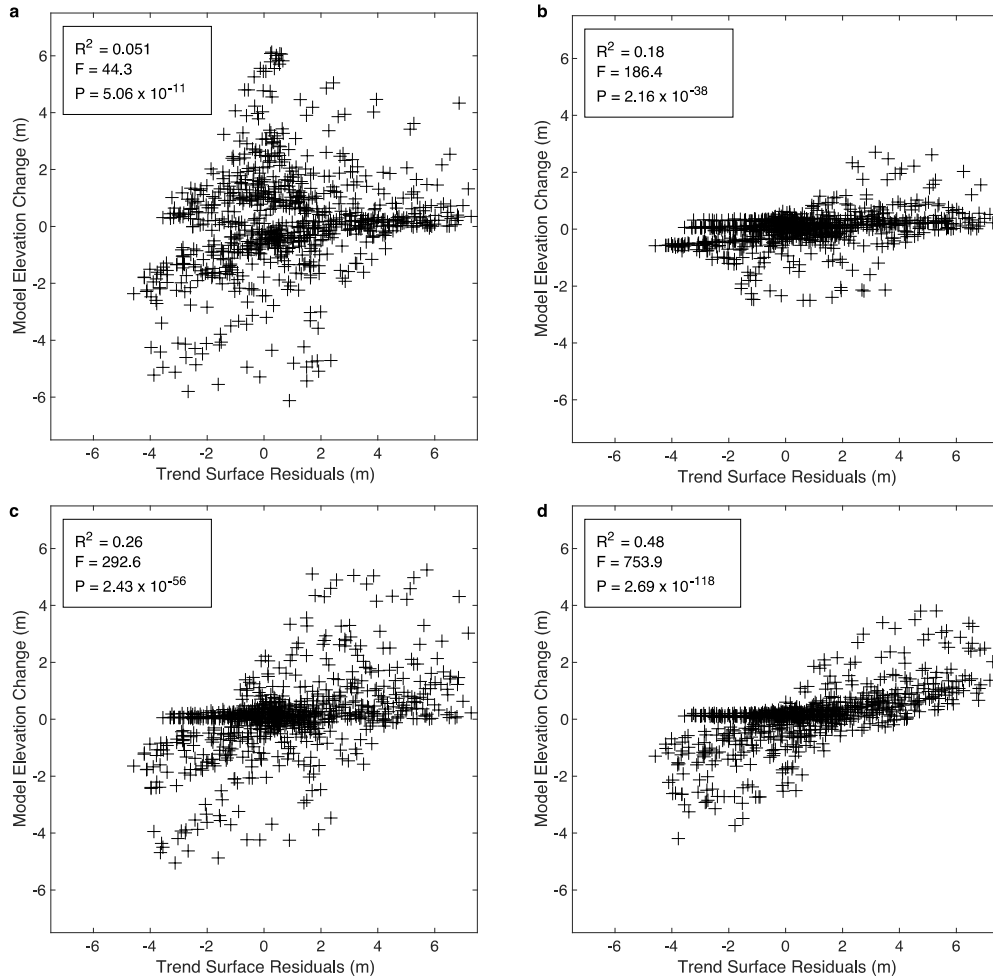


Figure 3. Scatter plots of residuals from trend surface shown in Figure 1d against modelled elevation changes within 20 km radius of the centre of the region containing the inferred water. Trend surface residuals are at the nearest MOLA grid point to modelled grid points. **a.** Run M1. **b.** Run S9. **c.** Run C6. **d.** Run LL6. Ordinary least squares regression results for modelled height change versus trend surface residuals are given as the R^2 statistic, the F statistic for a significant linear regression relationship, and the P-value for F. In all cases, $n = 824$, $DF = 822$.

450 References

- 451 1. Orosei, R. *et al.* Radar evidence of subglacial liquid water on Mars.
452 *Science* **361**, 490–493 (2018).
- 453 2. Lauro, S. E. *et al.* Multiple subglacial water bodies below the south pole
454 of Mars unveiled by new MARSIS data. *Nat. Astron.* **5**, 63–70 (2021).
- 455 3. Khuller, A. R. & Plaut, J. J. Characteristics of the Basal Interface of the
456 Martian South Polar Layered Deposits. *Geophys. Res. Lett.* (2021)
457 doi:10.1029/2021GL093631.
- 458 4. Bierson, C. J., Tulaczyk, S., Courville, S. W. & Putzig, N. E. Strong
459 MARSIS Radar Reflections from the Base of Martian South Polar Cap
460 may be due to Conductive Ice or Minerals. *Geophys. Res. Lett.* (2021)
461 doi:10.1029/2021GL093880.
- 462 5. Smith, I. B. *et al.* A Solid Interpretation of Bright Radar Reflectors
463 Under the Mars South Polar Ice. *Geophys. Res. Lett.* (2021)
464 doi:10.1029/2021GL093618.
- 465 6. Grima, C., Mouginot, J., Kofman, W., Hérique, A. & Beck, P. The Basal
466 Detectability of an Ice-Covered Mars by MARSIS. *Geophys. Res. Lett.*
467 **49**, (2022).
- 468 7. Ridley, J. K., Cudlip, W. & Laxon, S. W. Identification of subglacial lakes
469 using ERS-1 radar altimeter. *J. Glaciol.* **39**, 625–634 (1993).
- 470 8. Smith, D. E. *et al.* Mars Orbiter Laser Altimeter: Experiment summary
471 after the first year of global mapping of Mars. *J. Geophys. Res. Planets*
472 **106**, 23689–23722 (2001).
- 473 9. Sori, M. M. & Bramson, A. M. Water on Mars, with a grain of salt: local
474 heat anomalies are required for basal melting of ice at the south pole
475 today. *Geophys. Res. Lett.* **46**, 1222–1231 (2019).
- 476 10. Butcher, F. E. G. *et al.* Recent basal melting of a mid-latitude glacier
477 on Mars. *J. Geophys. Res. Planets* **122**, 2445–2468 (2017).
- 478 11. Livingstone, S. J. *et al.* Subglacial lakes and their changing role in a
479 warming climate. *Nat. Rev. Earth Environ.* **3**, 106–124 (2022).
- 480 12. Butcher, F. E. G., Conway, S. J. & Arnold, N. S. Are the Dorsa
481 Argentea on Mars eskers? *Icarus* **275**, 65–84 (2016).
- 482 13. Head, J. W. & Pratt, S. Extensive Hesperian-aged south polar ice
483 sheet on Mars: Evidence for massive melting and retreat, and lateral
484 flow and ponding of meltwater. *J. Geophys. Res. Planets* **106**, 12275–
485 12299 (2001).
- 486 14. Gallagher, C. & Balme, M. Eskers in a complete, wet-based glacial
487 system in the Phlegra Montes region, Mars. *Earth Planet. Sci. Lett.* **431**,
488 96–109 (2015).

15. Butcher, F. E. G. *et al.* Sinuous ridges in Chukhung crater, Tempe Terra, Mars: Implications for fluvial, glacial, and glaciofluvial activity. *Icarus* **357**, 114131 (2021).
16. Mattei, E. *et al.* Assessing the role of clay and salts on the origin of MARSIS basal bright reflections. *Earth Planet. Sci. Lett.* **579**, 117370 (2022).
17. Remy, F., Mazzega, P., Houry, S., Brossier, C. & Minster, J. F. Mapping of the Topography of Continental Ice by Inversion of Satellite-altimeter Data. *J. Glaciol.* **35**, 98–107 (1989).
18. Mantripp, D. N., Ridley, J. K. & Rapley, C. G. Antarctic map from the Geosat Radar Altimeter Geodetic Mission. *Earth Obs. Quarterly* **37–38**, 6–10 (1992).
19. Grima, C. *et al.* Large asymmetric polar scarps on Planum Australe, Mars: Characterization and evolution. *Icarus* **212**, 96–109 (2011).
20. Kennelly, P. J. Terrain maps displaying hill-shading with curvature. *Geomorphology* **102**, 567–577 (2008).
21. Arnold, N. A new approach for dealing with depressions in digital elevation models when calculating flow accumulation values. *Prog. Phys. Geogr. Earth Environ.* **34**, 781–809 (2010).
22. Larour, E., Seroussi, H., Morlighem, M. & Rignot, E. Continental scale, high order, high spatial resolution, ice sheet modeling using the Ice Sheet System Model (ISSM). *J. Geophys. Res. Earth Surf.* **117**, (2012).
23. Arnold, N. S., Conway, S. J., Butcher, F. E. G. & Balme, M. R. Modeled Subglacial Water Flow Routing Supports Localized Intrusive Heating as a Possible Cause of Basal Melting of Mars' South Polar Ice Cap. *J. Geophys. Res. Planets* **124**, 2101–2116 (2019).
24. Herkenhoff, K. Surface Ages and Resurfacing Rates of the Polar Layered Deposits on Mars. *Icarus* **144**, 243–253 (2000).
25. Koutnik, M., Byrne, S. & Murray, B. South Polar Layered Deposits of Mars: The cratering record: SOUTH POLAR LAYERED DEPOSITS OF MARS. *J. Geophys. Res. Planets* **107**, 10-1-10-10 (2002).
26. Plaut, J. J. *et al.* Subsurface radar sounding of the south polar layered deposits of Mars. *Science* **316**, 92–95 (2007).
27. Tanaka, K. L. *et al.* *Geologic map of Mars*. 48 <http://pubs.er.usgs.gov/publication/sim3292> (2014).
28. Pattyn, F., Smedt, B. D. & Souchez, R. Influence of subglacial Vostok lake on the regional ice dynamics of the Antarctic ice sheet: a model study. *J. Glaciol.* **50**, 583–589 (2004).
29. Fisher, D. A., Hecht, M. H., Kounaves, S. P. & Catling, D. C. A perchlorate brine lubricated deformable bed facilitating flow of the north

530 polar cap of Mars: Possible mechanism for water table recharging. *J.*
531 *Geophys. Res.* **115**, (2010).
532